Rotary regenerative shock absorbers for automotive suspensions

Rotary regenerative shock absorbers for automotive suspensions

Renato Galluzzi[a,*], Salvatore Circosta[a], Nicola Amati[a], Andrea Tonoli[a]

[a]*Department of Mechanical and Aerospace Engineering, Politecnico di Torino, Corso Duca degli Abruzzi, 24, Turin, Italy*

Abstract

The increasingly strict limits on pollutant emissions are pushing the car industry towards the electrification of the powertrain and chassis. This scenario has driven the automotive field to the use of energy harvesters. Among these, regenerative shock absorbers are mechatronic devices that enable the energy recovery from road irregularities, thus yielding benefits in terms of fuel saving and ride quality. The state of the art proposes different technologies for regenerative dampers. In this context, rotary dampers represent an unexplored field from the scientific point of view. This work proposes the system-level design of a rotary regenerative shock absorber for automotive suspensions, which features a leverage and a planetary gearbox to convert the suspension linear motion into rotation of an electric machine. Firstly, we define the fundamental design and integration aspects of the device: electric machine, leverage and gearbox. Then, we verify the prototype performance in terms of damping capability, efficiency and acoustic behavior.

Keywords: regenerative, energy harvesting, gearbox, damper, rotary

1. Introduction

The electrification of automotive systems is an ongoing evolving effort, with new regulations worldwide driving the change for a cleaner environment [1]. In this scenario, mechatronic devices with energy harvesting features are favored due to their improved efficiency and reduced CO_2 footprint. Regenerative shock absorbers are one of such technologies. These systems are able to yield damping or even active forces to the vehicle suspension, while also recovering part of the energy otherwise dissipated as heat [2]. For this purpose, they employ an electric machine controlled as a generator (damper) or motor (actuator).

Abdelkareem *et al.* have performed a detailed review on automotive vibration energy harvesting [3] by dealing with global energy aspects and the different technologies to perform regenerative shock absorption. They have highlighted benefits in terms of fuel saved, ride comfort, road holding and CO_2 emission reduction. All these aspects are strongly dependent on the technology adopted to transfer the road unevenness to the electric machine.

Due to the nature of the suspension motion, linear electric machines seem a straightforward candidate for regenerative damping [4]. However, their limited force density suggests the use of rotary electric motors combined with a suitable linear-to-rotary conversion system [5]. Ball screw [6–8], rack pinion [9, 10] and electro-hydrostatic transmissions [11–13] are some of the main examples found in the literature.

In 2016, Audi AG introduced eROT, a novel concept of regenerative suspension based on a rotary drive: electric machine and gearbox [14, 15]. Unlike traditional dampers, this system is connected to the suspension by means of a leverage. The device is able to work as a full active damper. Audi AG specified a total harvesting output from four corners between 100 and 150 W on average during testing on German roads. Power transients go from 3 W on a freshly paved motorway to 613 W on a rough secondary road. Under customer driving conditions, this corresponds to CO_2 savings of up to 3 g/km.

*Corresponding author
Email addresses: renato.galluzzi@polito.it (Renato Galluzzi), salvatore.circosta@polito.it (Salvatore Circosta), nicola.amati@polito.it (Nicola Amati), andrea.tonoli@polito.it (Andrea Tonoli)

Nomenclature

a	center distance
$a_{1,i}$	number of load cycles at continuous rotation (ith gear)
$a_{2,i}$	correction coefficient for alternate bending (ith gear)
b	tooth face width
c_e	electromagnetic viscous damping
c_{eq}	suspension equivalent viscous damping
c_l	suspension short-circuit viscous damping in the linear domain
c_m	viscous damping at the electric machine level
k_f	slot fill factor
k_s	suspension stiffness
k_u	tire stiffness
l_{et}	end-turn length
l_m	active length
m_{eq}	suspension equivalent mass
m_n	normal module
m_s	sprung mass
m_u	unsprung mass
p	number of pole pairs
p_0	reference pressure
p_A	acoustic pressure
r_{Tl}	torque-to-length ratio
s	Laplace variable
t	time
v	suspension linear speed
z	number of teeth
A_s	slot cross section
A_w	wire cross section
D_{so}	stator outside diameter
F	suspension force
F_{rms}	suspension root-mean-square (RMS) force
G_r	road roughness index
H_r	filtering function for road profile synthesis
H_A	A-weighting filtering function
I_{ph}	phase current amplitude
J_{in}	moment of inertia at the gearbox input shaft level
J_m	moment of inertia at the electric machine level
J_{rms}	wire root-mean-square (RMS) current density
K_e	back electromotive force (EMF) constant
K_t	torque constant
K_A	application factor
K_V	dynamic load factor
K_α	transverse load factor
L	inductance in d and q axes
N_c	number of coils in series per phase
N_i	number of load cycles (ith gear)
N_s	number of slots
N_t	number of turns per coil
R	phase resistance
R_s	shunt resistance
SPL	sound pressure level
T	input shaft torque
T_m	electric machine torque
$T_{m,cont}$	electric machine torque, continuous output
$T_{m,imp}$	electric machine torque, impulsive output
V_{car}	vehicle speed
V_{dc}	direct-current (DC) link voltage
V_s	shunt resistance voltage
Y_m	alternating bending factor
α	pressure angle
η	conversion efficiency
ρ_{Cu}	copper resistivity
τ_g	gearbox transmission ratio
τ_i	transmission ratio between input stage and ith gear
τ_l	leverage transmission ratio
τ_t	total transmission ratio
χ^*	profile shift coefficient
ω	input shaft angular speed
ω_0	road profile filter cutoff frequency
ω_m	electric machine angular speed
ω_p	electromagnetic pole frequency

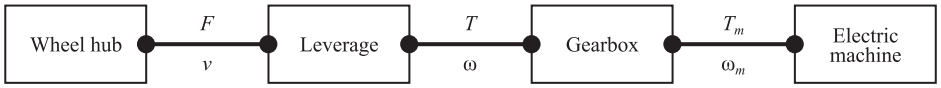

Figure 1: Rotary regenerative shock absorber working principle diagram.

Latest developments from Audi AG show a similar device that can be actively operated to further improve comfort and safety. A predictive control strategy employs a camera to scan road unevenness so that the active suspension is regulated to make the cruise smoother. If a hazardous situation around the vehicle is identified, the active suspension raises the car body to improve the impact energy absorption capability. Furthermore, longitudinal and lateral acceleration felt by the passengers can be reduced by opportunely tilting the car body when entering a corner or during a hard braking [16].

Also, other car manufacturers like Hyundai [17] and Honda [18] are investing in the development of rotary dampers. This background demonstrates that the topic is currently of great interest to the automotive industry. However, despite the promising performance numbers, literature in the field has not addressed properly the rotary damper technology. When understanding how rotary regenerative dampers compare with other technologies, many questions arise: What energy efficiency can we expect from these devices? How should the engineer address the design? What are the potential drawbacks?

The present work aims to address these open points. The methodology proposed in sec. 2 addresses the design of a rotary regenerative shock absorber at a system level. The electric machine inside the device is designed on the base of damping specifications, geometry and heat dissipation capability. The damper duty cycle is generated using a quarter-car model running through a realistic worst-case mission profile. This allows proper sizing of the electric machine and the gearbox transmission ratio.

Then, we define the placement of the damper inside the vehicle and the leverage needed to convert the linear motion of the wheel upright into angular displacement. This step is driven by packaging and performance considerations.

Subsequently, the gearbox design is addressed. The available literature in this subject is extensive [19, 20]. Recent works have covered energy conversion applications in the wind power field [21, 22]. In this context, we focus on the definition of the external loads acting on the components. The input load spectrum is extracted from the same quarter-car model simulations used to size the electric machine.

Finally, sec. 3 deals with the performance assessment of a rotary regenerative shock absorber. Damping capability, efficiency and noise levels are evaluated in an experimental campaign. Experimental results are aimed also to unify the design methodology.

2. Design

The Rotary Regenerative Shock Absorber (RRSA) treated in this study exploits a suitably controlled electric machine that provides a force that aids or counteracts the suspension linear motion. In the former case, the machine acts as a motor by actively drawing power from its supply to exert mechanical power. In the latter, the machine can potentially perform mechanical-to-electrical power conversion. Hence, kinetic energy from road irregularities can be stored as electricity in a battery.

A leverage is used to convert linear motion into angular displacement. As schematized in Fig. 1, the wheel upright linear speed (v) is transformed into rotary motion (ω) by means of a leverage, which introduces a transmission ratio $\tau_l = v/\omega$. During damping operation, the angular speed ω is applied to the low-speed high-torque shaft of the gearbox, while its high-speed low-torque shaft is coupled to the rotor of an electric machine. Therefore, the gearbox operates as a speed multiplier with a transmission ratio $\tau_g = \omega/\omega_m$, where ω_m is the angular speed of the electric machine.

The overall transmission ratio τ_t is defined as the ratio between the suspension linear speed and the electric machine angular speed:

$$\tau_t = \tau_l \tau_g = \frac{v}{\omega_m} \tag{1}$$

The ratio τ_t is a relevant design parameter: it has an impact on the size of the electric machine. Considering an ideally static transmission, the electric machine torque is given by

$$T_m = \tau_t F \tag{2}$$

where F is the input force at the suspension. By converse, any inertial (J_m) or dissipative contribution in the form of damping (c_m) at the level of the electric machine is seen by the suspension as

$$c_{eq} = c_m/\tau_t^2 \tag{3}$$

$$m_{eq} = J_m/\tau_t^2 \tag{4}$$

Thus, small values of τ_t favor compact machines with low torque capability, while increasing friction loss effects due to larger equivalent damping c_{eq}. Although mechanical losses contribute to the suspension damping effect, they reduce the conversion efficiency of the device. The equivalent inertia m_{eq} follows a similar trend when τ_t changes. Inertial contributions play a relevant dynamic role, as they tends to stiffen and lock the suspension when subject to high-frequency excitation [5, 8].

On the contrary, when large transmission ratio values are used, performance improves at the cost of increasing the torque demand and hence, the size of the electric machine.

2.1. Electric machine design

The electric machine technology and its design are defined by operating conditions within different physical domains, i.e. mechanical (level of vibrations), electrical (voltage and current limitations) and thermal (temperature). Since compactness is crucial in this application, the permanent-magnet synchronous machine is selected because it offers the highest torque-to-mass ratio among electric motors.

The sizing of the electric machine is strictly related to the definition of the overall transmission ratio. The latter allows translating the requirements at the wheel upright into the input of the electric machine. The design method is divided into two sequential steps:

1. Sizing of the electric machine cross section.
2. Definition of the machine active length and the overall transmission ratio.

To start the design, we first constrain the stator outside diameter D_{so} to a value that suits the available space within the suspension. This allows defining the cross section of the electric machine. For this purpose, a permanent-magnet synchronous motor is designed with the final goal of maximizing its output torque-to-length ratio r_{Tl}. This step can be achieved either by analytical means or through finite-element models [23]. In this procedure, each phase of the machine is fed by a balanced sinusoidal current density waveform. The root-mean-square (RMS) value of the wire current density should match $J_{rms} = 6\,\mathrm{A/mm^2}$ to allow continuous operation within safe thermal behavior [24].

As a second step, the design method requires the machine active length l_m and the overall transmission ratio τ_t. To determine these quantities, we first define the maximum damping target reported in Fig. 2. This characteristic belongs to a crossover SUV; it is a piecewise linear function with a first damping slope of 10 kNs/m up to 1 kN of force and 0.1 m/s of speed. Afterwards, the slope becomes less steep: 0.53 kNs/m.

The suspension force reaction is computed by means of a quarter-car model populated by the parameters in Tab. 1. The damper is modeled through the nonlinear force-speed mapping depicted in Fig. 2. The external excitation is an ISO-B road profile [25]. As suggested in the literature [26], the road profile time history is synthesized with a unit-power white noise input and the following filtering function:

$$H_r(s) = \frac{2\pi\sqrt{G_r V_{car}}}{s + \omega_0} \tag{5}$$

where $G_r = 6.4 \cdot 10^{-7}\,\mathrm{m \cdot cycle}$ is the road roughness index, $V_{car} = 70\,\mathrm{km/h}$ is the vehicle speed and $\omega_0 = 1.22\,\mathrm{rad/s}$ is the cutoff frequency. The model is simulated for ten seconds to reproduce dynamic behavior more than one decade below the slowest dynamics on the system, namely that of the sprung mass (1.2 Hz). After the simulation, the time history of the damping force can be extracted, and its RMS value (F_{rms}) can be calculated.

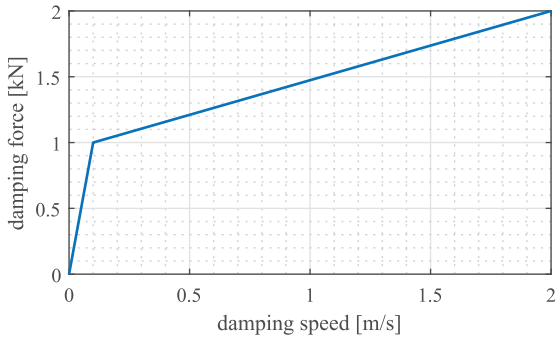

Figure 2: Maximum damping specification for one corner of a crossover SUV. The characteristic is symmetric, only one quadrant is reported.

Table 1: Quarter-car model parameters for a crossover SUV.

Description	Symbol	Value
Sprung mass	m_s	417 kg
Unsprung mass	m_u	40 kg
Suspension stiffness	k_s	23 kN/m
Tire stiffness	k_u	226 kN/m

The continuous torque of the machine is given by

$$T_{m,cont} = r_{Tl} l_m = \tau_t F_{rms} \tag{6}$$

which means that the machine should operate continuously at the given load conditions. Note that Eq. (6) assumes unitary efficiency of the gearbox and the lever transmission. This is a worst-case scenario from the electric machine perspective because it should supply all the required damping torque.

The maximum damping coefficient dictates a further constraint: the electric machine should be able to yield the largest damping coefficient without providing any active power to the system.

As stated in [5, 27, 28], a shunted brushless PM machine exhibits a well-known electromagnetic torque versus angular speed characteristic described by

$$T_m = \frac{3K_e^2 \omega_m}{2\,(R + R_s)\left[1 + \left(p\omega_m/\omega_p\right)^2\right]} \tag{7}$$

where K_e is the machine back electromotive force (EMF) constant, R is its phase resistance and R_s is the load that shunts the windings. The angular frequency ω_p represents an electromagnetic pole defined by

$$\omega_p = \frac{R + R_s}{L} \tag{8}$$

with L being the machine inductance in d and q axes.

Note that low values of angular speed ($\omega_m \ll \omega_p/p$) yield a viscous damping characteristic approximated by

$$T_m \cong \frac{3K_e^2}{2\,(R + R_s)} \omega_m \tag{9}$$

where the electromagnetic viscous damping in the rotary domain can be approximated as

$$c_e = \frac{3K_e^2}{2\,(R + R_s)} \tag{10}$$

The maximum damping capability is obtained when $R_s = 0$. This short-circuit damping value can be written in the linear domain as a function of the torque constant $K_t = 2K_e/3$ [29]:

$$c_l = \frac{2K_t^2}{3\tau_t^2 R} \tag{11}$$

The phase resistance is given by

$$R = \frac{2N_c N_t \rho_{Cu}}{A_w} (l_m + l_{et}) \tag{12}$$

where N_c is the number of coils in series per phase, N_t is the number of turns per coil, ρ_{Cu} is the electrical resistivity of copper and l_{et} is the length of the end-turn path. The wire cross section A_w can be expressed as a function of the machine slot cross section A_s, since

$$A_w = \frac{k_f A_s}{N_t} \tag{13}$$

being k_f the slot fill factor.

The torque constant, instead, is given by the ratio between the continuous torque $T_{m,cont}$ and the phase current amplitude I_{ph}, but it can be expressed as a function of the wire RMS current density:

$$K_t = \frac{T_{m,cont}}{I_{ph}} = \frac{r_{Tl} l_m}{\sqrt{2} J_{rms} A_w} \tag{14}$$

It is seen from Eq. (6) that the active length l_m is a linear function of the transmission ratio τ_t, since

$$l_m = \frac{F_{rms}}{r_{Tl}} \tau_t \tag{15}$$

Substituting Eqs. (6) and (12) to (15) into (11) yields the maximum damping as a function of the transmission ratio τ_t and a set of known parameters:

$$c_l = \frac{F_{rms}^2}{6 J_{rms}^2 A_s k_f N_c \rho_{Cu} \left(\frac{F_{rms}}{r_{Tl}} \tau_t + l_{et} \right)} \tag{16}$$

Equation (16) can be solved for τ_t to yield a given maximum damping specification c_l. Furthermore, this transmission ratio is also used to determine the active length of the machine by substituting it into Eq. (15).

The electric machine cross section was optimized through finite-element simulations using the AC/DC module of COMSOL Multiphysics. A machine geometry with a stator outside diameter of 70 mm, twelve slots and five pole pairs was iteratively refined to maximize the output torque while fed by $J_{rms} = 6\,\mathrm{A/mm^2}$. The average flux density in the back iron and the teeth was carefully monitored in this process to avoid magnetic saturation and hence, efficiency loss.

Figure 3 illustrates the sizing of the electric machine axial length ($l_m = 22$ mm) and the overall transmission ratio ($\tau_t = 1.35$ mm/rad). In this case, the maximum damping coefficient requirement was set to $c_l = 20$ kNs/m to account for additional losses introduced by the power stage controlling the machine.

Finally, the designer should assess whether the machine can yield the maximum damping force, although this operation is of intermittent nature ($t < 1$ s). The parameters of the designed machine are listed in Tab. 2.

2.2. Leverage definition and system integration

The leverage design is heavily guided by the vehicle suspension layout. In the present paper, a double wishbone front suspension is considered as a reference architecture. Therefore, the damper tube does not accomplish major structural function. In a future perspective, this tube could be completely replaced by the RRSA if a proper alternative connection to the spring element is found.

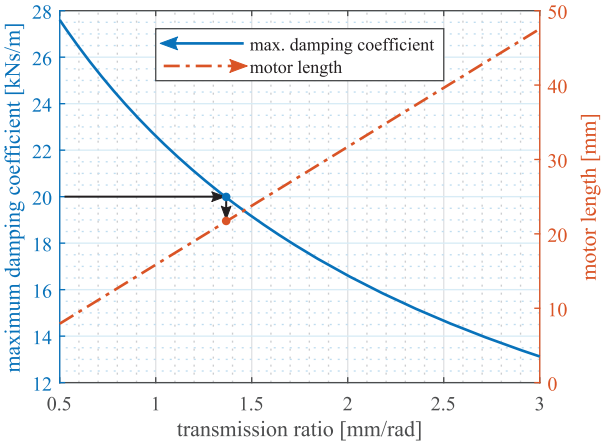

Figure 3: Selection of the overall transmission ratio τ_t as a function of the maximum damping coefficient c_l. The selection of τ_t leads to the electric machine active length l_m.

The suspension kinematics is simplified into a 2D representation and the linkages are studied with the mechanism synthesis approach, as seen in Fig. 4. The lever transmission ratio τ_l and the transmission angle are the performance parameters considered in the definition of the leverage. The lever transmission ratio translates the linear speed applied at the upright (v) into an angular speed at the gearbox input shaft (ω). Correspondingly, the electric machine reacts by yielding a torque T at the gearbox input shaft, which will be converted into a force F at the upright. The ratio τ_l must be minimized so that, according to Eq. (1), the overall transmission ratio τ_t can be achieved with a lower gearbox contribution τ_g. This improves both the compactness and the efficiency of the gearbox.

The transmission angle defines the quality of the leverage transmission. In the case of a four-bar linkage, it is defined as the angle between the coupler and the follower. It varies throughout the range of operation and is most favorable when equal to 90°. Therefore, the design aims to limit the transmission angle in the range between 40° and 140°, as recommended in the literature [30].

The fulfillment of performance and packaging criteria leads to the four layouts illustrated in Fig. 4. Layouts (a) and (b) place the RRSA in the pivot point of the lower and the upper suspension arm, respectively. No additional levers are needed, since the suspension arms themselves are used as links. Both layouts offer a simple solution since the suspension architecture remains unchanged. However, the resulting leverage transmission ratio is 346 mm/rad for Layout (a) and 251 mm/rad for Layout (b). Layout (c) decreases the leverage transmission ratio through a four-bar linkage constituted by the lower suspension arm and two additional links. Such leverage achieves a nominal transmission ratio of 100 mm/rad. Layout (d) uses two links, where the longest one is hinged on the damper tube. The RRSA is placed at the pivot point of the lower arm, thus yielding a nominal transmission ratio of 115 mm/rad. Among the investigated configurations, Layout (c) achieves the lowest τ_l and therefore, constitutes a promising candidate in the case of a total redesign of the suspension architecture. Layout (d), on the other hand, features a slightly larger transmission ratio than (c), but does not require significant changes in the existing suspension assembly. Therefore, Layout (d) is taken as reference setup for the design of the gearbox.

Hence, this application addresses an RRSA design based on a leverage system able to accomplish a transmission of 115 mm/rad. The layout of this mechanism is constrained by the suspension architecture.

2.3. Gearbox design

The selection of the gearbox architecture was driven by envelope constraints. Fixed-axis and planetary configurations were compared and, although the former achieves slightly better performance in terms of noise level and efficiency, the planetary architecture features significant compactness and reduced mass. Hence, a planetary gearbox was chosen for the present application.

The selected configuration features two stages that share the same fixed ring, as depicted in Fig. 5. Each stage has one planet carrier, three planet gears and a sun gear. For each of both stages, the input is fixed to the planet carrier, whereas the sun gear represents the output. The output of the second stage drives the electric machine shaft.

Table 2: Electric machine main features.

Description	Symbol	Value
Stator outside diameter	D_{so}	70 mm
Active length	l_m	22 mm
Number of slots	N_s	12
Number of pole pairs	p	5
Phase resistance	R	20 mΩ
Inductance in d and q axes	L	85 μH
Back EMF constant	K_e	21 mVs/rad
Slot fill factor	k_f	0.3
Slot cross section	A_s	118 mm^2
End-turn length	l_{et}	28 mm
Copper resistivity	ρ_{Cu}	$1.68 \cdot 10^{-8}$ Ωm
Number of coils in series per phase	N_c	2
Nominal DC link voltage	V_{dc}	48 V
Continuous torque-to-length ratio	r_{Tl}	31.8 Nm/m
Continuous torque output	$T_{m,cont}$	0.7 Nm
Impulsive torque output ($t < 1$ s)	$T_{m,imp}$	2.7 Nm

The design goal is the optimization of the selected configuration by attempting to minimize mass and overall dimensions, as well as the gearbox inertia at the input shaft. Gearbox components must be sized to withstand overloads and fatigue. The operating conditions are defined at the suspension level, hence the leverage transmission ratio τ_l is used to convert them to the gearbox input shaft.

The overload condition is obtained from the maximum damping characteristic in Fig. 2. This specification is a reasonable assumption for a crossover SUV-class vehicle [31]. The maximum load of the characteristic is rarely reached, therefore the point (2 m/s, 2 kN) is a worst case. It corresponds to 166 rpm and 230 Nm at the gearbox input.

A more realistic overload condition is represented by a bump of height 20 mm when the vehicle travels at 70 km/h. This can be obtained through a quarter-car model simulation (see sec. 2.1), where the external excitation is the bump profile. This leads to a peak damping force of 1.32 kN at 0.67 m/s, thus yielding 151.4 Nm and 55.4 rpm at the gearbox input shaft. Since this situation is less demanding than the maximum load of the damping characteristic, the latter is still considered as a conservative condition.

The fatigue load spectra (damping torque and speed) are obtained using the same quarter-car model running through an ISO-B road profile at 70 km/h. From the obtained results, the ordinate axis of the load time history is discretized into 10 Nm-wide intervals. The duty cycle is calculated as the time fraction in which the device operates inside each load interval with respect to the total simulation time. Then, these load bins are translated to their speed counterpart through the damping characteristic in Fig. 2. The resulting spectra are shown in Fig. 6.

2.3.1. Gear sizing

The sizing of the planetary sets with cylindrical gears obeys the ISO 6336 method B [32–35].

The following constraints are considered in the design:

1. Gearbox transmission ratio τ_g in the range $1/96 \div 1/77$, in agreement with the selected leverage and the electric machine requirement (see sec. 2.1).
2. Transmission ratio equally split between the two stages.
3. Diameter envelope upper bound of 100 mm to mechanically fit the gearbox to the outside diameter of the electric machine stator (see Tab. 2).
4. 3600 h as reference life for fatigue sizing, which corresponds to 250 000 km for a vehicle travelling at 70 km/h.

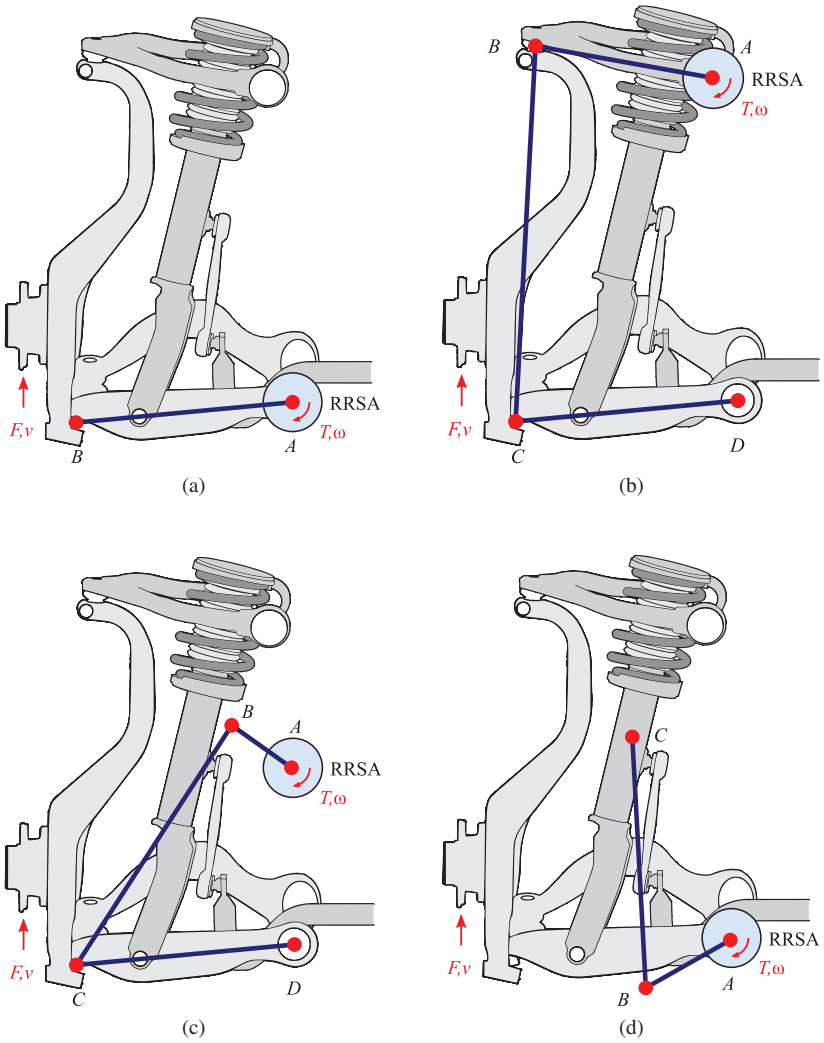

Figure 4: Proposed leverage solutions (thick solid lines) for the rotary regenerative shock absorber integration into a double wishbone suspension.

The load conditions at the input shaft, as defined in sec. 2.3, must be corrected to account for non-ideal operation [32–36]. Firstly, the dynamic load factor K_V and the transverse load factor K_α must be calculated according to the ISO standard [32]. The face load factor K_β, which accounts for uneven load distribution along the tooth face-width, must be considered if the maximum tilt of the planet axis is non-negligible. In this case, the tilt is constrained to 1 μm at the worst-case condition. In fact, the carriers were designed and validated through structural finite-element calculations to guarantee this deflection. Finally, the application factor is set to $K_A = 1$ for fatigue analysis as requested by the standard [35]. The same can be assumed for the static case since the considered overload condition is largely conservative.

Some considerations are needed for the alternating bending factor Y_m. It is set to 0.7 for the planets since they experience alternate bending every cycle and, in the case of constant angular motion, it is set to 1 for both the sun and the ring. In the considered fatigue condition, the gearbox input shaft does not experience complete rotations: it rather spans angular regions within ±15°. This forward/backward movement leads to alternate bending of sun and ring teeth.

Consequently, the following procedure is applied. At first, the factor Y_m is set to 0.7 for sun, ring and planets.

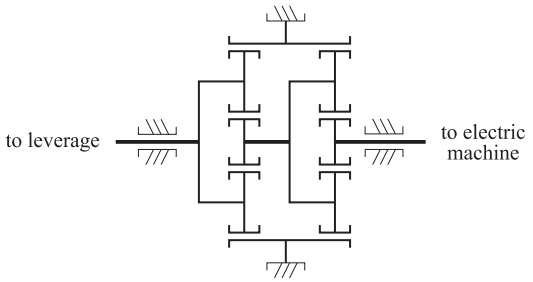

Figure 5: Gearbox scheme for rotary regenerative shock absorber.

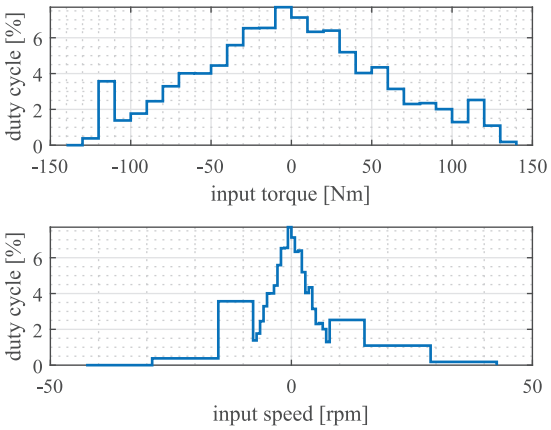

Figure 6: Load spectra for gearbox input torque (top) and input speed (bottom) calculated in a quarter-car model with the maximum damping characteristic (Fig. 2) running through an ISO-B road profile at 70 km/h.

Then, the equivalent number of load cycles per revolution of the generic ith gear is computed according to

$$N_i = a_{1,i} \cdot a_{2,i} \cdot \max\left(1, \frac{360}{\Delta\theta\tau_i}\right) \tag{17}$$

where τ_i is the transmission ratio between the input of the stage and the ith gear, $\Delta\theta$ is the angular region spanned by the input shaft of the stage, $a_{1,i}$ is the number of load cycles of the ith gear in the case of continuous rotation. The latter is equal to 3 for the sun and ring, and 1 for the planets. Coefficient $a_{2,i}$ considers that sun and ring experience one complete alternate bending cycle in two revolutions (one forward and one backward), not in one as considered by $Y_m = 0.7$. Therefore, coefficient $a_{2,i}$ is set to 0.5 for the sun and ring in order to halve the number of cycles per revolution, while it is kept unitary for the planets.

The gears are designed by means of the commercial software KISSsoft, a tool for performing sizing calculations of machine elements according to industrial standards [37]. The software performs both static and fatigue design in two routines. At first, a rough sizing returns several configurations that satisfy the required transmission ratio and the radial envelope within a certain range. Then, the selected configuration undergoes a fine sizing that fully defines the gear set and returns several possible solutions. The optimal one is chosen by comparing different parameters such as mass, equivalent inertia at the input shaft, efficiency and safety factors. The selected configuration is reported in Tab. 3. The two stages have the same features, except for the tooth face width, which is shorter for the second stage. This enables a significant reduction of the gearbox inertia, mass and bulk. Both stages feature a transmission ratio of 9.346, yielding a gearbox transmission ratio $\tau_g = 1/87.35$. Gears are made of steel grade 3 AGMA 2001 C95. In the worst case, the fatigue load spectrum leads to a safety factor of 1.1 for the bending strength at the tooth root (first stage).

Table 3: Gear characteristics.

Description	Symbol	Value
Normal module	m_n	0.6 mm
Pressure angle	α	20°
Center distance	a	22.5 mm
Number of teeth, sun	z_{sun}	16
Number of teeth, planet	z_{planet}	58
Number of teeth, ring	z_{ring}	−134
Profile shift coefficient, sun	χ^*_{sun}	0.459
Profile shift coefficient, planet	χ^*_{planet}	0.065
Profile shift coefficient, ring	χ^*_{ring}	0.409
Tooth face width, first stage	b_1	15 mm
Tooth face width, second stage	b_2	5 mm

2.4. Prototype assembly

Once the gears are sized, the gearbox assembly in Fig. 7 is defined. The suns of both stages (2,3) are machined on their respective shafts. The ring (10) is an external gear whose outer diameter is constrained by minimum rim thickness (1.2 times the tooth height). Therefore, the ring external diameter is set to 85.5 mm, which satisfies the diameter envelope constraint (sec. 2.3.1).

The gearbox multiplier configuration is displayed in detail in Fig. 8. All planet gears (17,19) are machined to house a bearing whose inner ring is supported by a pin (15,21). First-stage planets mount needle cage roller bearings (16), whereas ball bearings (20) are used for the second stage. Pins and carriers are optimized to reduce the stage inertia and keep the pin deflection below 1 μm at the bump loading condition. This constraint derives from gear meshing requirements (sec. 2.3.1). First-stage pins work as the inner raceway for the needle cage roller bearings. Therefore 18CrNiMo7-6—a case hardening steel alloy—is used. Steel grade 3 AGMA 2001 C95 is chosen for the carriers (14,23). The latter are constituted by two flanges bolted through calibrated screws. This layout makes the structure stiffer and enables the reduction of pin deflection.

The input shaft tip presents a splined profile (1) to couple with the leverage. Since the shaft has one support only, the bearing is subject to bending load caused by the axial misalignment between the leverage input force and the support. Therefore, a double-row angular contact ball bearing with a single piece inner ring is selected (13).

The external casing is made of Series 5 aluminum alloy. It consists of two parts: the front cover (12) and the gearbox casing (11). The latter is interfaced with the custom brushless PM machine body (4).

To favor compactness, the sun of the output stage is machined directly on the rotor of the electric motor (5), (22). This element is supported by two single-row ball bearings axially preloaded by a wave spring. The stator of the machine (9) is held inside its casing through a preload ring. For control purposes, the rotor end was equipped with a set of permanent magnets. Angular position is estimated by measuring their magnetic field with an array of Allegro A1326 analog Hall sensors (7) installed on the back cover (6).

2.5. Prototype features and expected performance

The designed RRSA weighs 3.2 kg, divided approximately into 1.5 kg of the gearbox and 1.7 kg of the electric machine assembly. The mass of the device, as conceived in the present configuration, contributes only to the sprung mass, since the actuator is attached to the chassis. To the actuator mass, one must add a mass component related to the lever arm (approximately 0.31 kg considering a steel part).

The moment of inertia at the gearbox input shaft is $J_{in} = 0.21\,\mathrm{kgm}^2$. By means of the leverage transmission, this inertial term contributes to the unsprung mass in dynamic conditions:

$$m_{eq} = J_{in}/\tau_l^2 = 15.9\,\mathrm{kg} \tag{18}$$

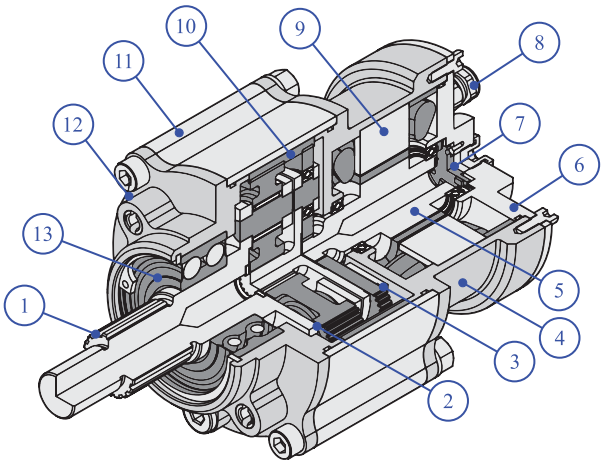

Figure 7: Isometric cut view of the rotary regenerative damper prototype: splined input shaft (1), first stage (2), second stage (3), motor casing (4), rotor (5), back cover (6), angular position sensor (7), cable gland [×4] (8), stator (9), outer ring gear (10), gearbox casing (11), front cover (12), input bearing (13).

This is a well-known drawback of electromagnetic shock absorbers that can be mitigated through active control.

The gearbox efficiency is evaluated at constant input torque and speed in the range from 20 to 180 Nm and 1 to 55.4 rpm. Calculations using KISSsoft yield efficiencies between 94% and 96%. By converse, the electric machine efficiency ranges from 0% to 85% according to finite-element simulations in COMSOL Multiphysics. Therefore, the RRSA efficiency is expected to be dominated by the electric machine.

3. Experimental results

3.1. Damping characterization

To validate the functionality of the RRSA, the test rig shown in Fig. 9 was devised. It consists of a driving motor (Kollmorgen DBL5-1700 brushless PM motor) and the RRSA prototype interfaced by means of a belt transmission with 2:1 ratio. A toothed belt (HTD-8M) was selected and properly preloaded to match a maximum input torque of 160 Nm for the prototype.

From the electrical point of view, the driving motor was connected to a dedicated inverter unit (Kollmorgen Servostar S748) to control its angular speed. The prototype was interfaced to a three-phase diode full bridge with a discretely-adjusted shunt resistance R_s. The variation of this resistive load allows setting different damping coefficients on the electric machine of the RRSA, as recalled from Eq. (7).

For the purposes of the application, the energy harvesting capability is particularly relevant. The power draw of the shunt resistance could be potentially harvested if an active power stage was used (for instance, a DC-DC converter after the diode bridge [11] or a three-phase MOSFET full bridge [12]). Although this power is dissipated, its measurement is useful to evaluate the conversion efficiency, i.e. the ratio between output electrical power and input mechanical power on the RRSA.

$$\eta = \frac{V_s^2}{R_s T \omega} \cdot 100\% \tag{19}$$

To assess both damping and conversion efficiency, the following measurements were extracted from the test rig:

1. The *driving motor current* measured through its inverter allows computing the input torque.
2. The *driving motor resolver signal* yields its angular speed.
3. The *shunt resistance voltage drop* is acquired using an oscilloscope voltage probe.

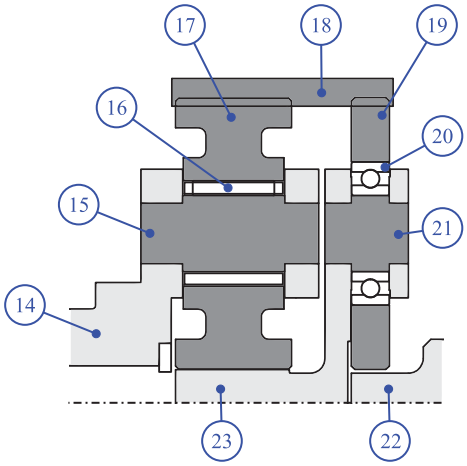

Figure 8: Side cut view of the gearbox multiplier. First stage: Input shaft/carrier (14), pin [×3] (15), needle bearing [×3] (16), planet [×3] (17). Second stage: Planet [×3] (19), ball bearing [×3] (20), pin [×3] (21), carrier (23). Outer ring gear (18), rotor (22).

Table 4: Damping feature comparison with different shunt resistance values.

Condition	Damping [kNs/m]		Speed that yields
	theory	measure fit	max. force [m/s]
$R_s \to \infty$	0	0.07	∞
$R_s = 465\,\mathrm{m\Omega}$	0.81	1.37	1.48
$R_s = 135\,\mathrm{m\Omega}$	2.53	3.38	0.47
$R_s = 55\,\mathrm{m\Omega}$	5.22	5.78	0.23
$R_s \to 0$	19.57	11.32	0.06
Max. specification	10	–	–

All these signals were fed into an LMS SCADAS data acquisition unit through 24-bit analogue channels opportunely scaled and sampled at 12.8 kHz.

In a typical test, the shunt resistance is fixed. Then, the driving motor is set to run at constant speed to avoid introducing inertial contributions from the motors or compliant effects from the belt transmission. Afterwards, measurement data are extracted.

Figure 10 depicts the damping characteristics of the RRSA attained with different shunt resistances: open circuit ($R_s \to \infty$), 465 mΩ, 135 mΩ, 55 mΩ and short circuit ($R_s \to 0$). Measured variables were converted to the linear domain (damping force and speed) to compare the obtained results with the maximum damping specification. The results confirm what expressed by Eq. (7): The behavior is predominantly viscous-dissipative and inversely proportional to the shunt resistance R_s, although slight attenuation is barely advisable towards high speeds.

Experimental results were subsequently fitted with first-degree polynomials. Table 4 lists the theoretical and fitted damping coefficients, as well as the damping speed at which the maximum force is reached: $\tau_t \omega_p / p$.

Some remarks must be made from these results. Since torque measurements are extracted from the driving motor current, they contain not only the electromagnetic damping component of the RRSA, but also the mechanical losses associated to the gearbox, the two pulleys and the driving motor bearings. On the other hand, diodes in the bridge introduce a nonlinear behavior characterized by a bias voltage drop of 0.4 V and a Joule effect loss that increases exponentially with current. These two effects combine: At low damping values, the mechanical loss contributions dominate, whereas the conduction losses penalize high-damping conditions, especially when in short circuit. Despite this limitation, the specified maximum characteristic slope is met. Furthermore, note that the diode bias voltage introduces a dead-band effect on the damping characteristic, i.e. curves tend to intersect the ordinate axis at negative

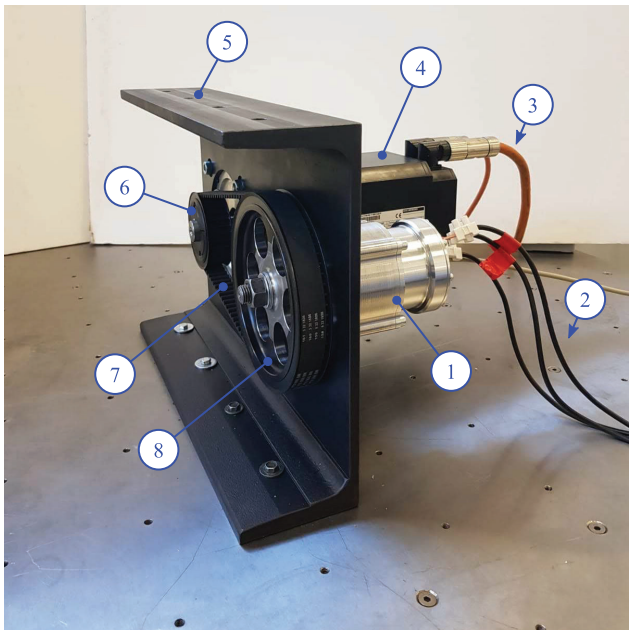

Figure 9: Experimental setup for damping and conversion efficiency characterization: rotary regenerative damper prototype (1), Prototype phases (2), driving motor phases and feedback (3), driving motor (4), test rig flange (5), driving pulley (6), belt (7), driven pulley (8).

force values.

From a practical standpoint, a controlled MOSFET power stage [12] would bring the following advantages:

- High efficiency in conduction and null offsets due to bias voltage.
- No torque attenuation due to inductive effect because the current control forces the current to flow in quadrature to the machine flux.
- Possibility of reproducing a piece-wise damping specification by simply limiting the motor current.

In terms of damping, the state of the art evaluates the damping-to-mass ratio as a meaningful performance parameter [5]. It highlights a maximum value of 2.44 kNs/(mkg). Experiments demonstrate that the RRSA prototype exceeds this number with a ratio of 3.23 kNs/(mkg) among different technologies. This advantage could be attributed to a reduced added mass and bulk of the rotary solution. However, this point could not be quantified properly, as the available literature does not report clear mass and geometric features.

3.2. Efficiency characterization

The results obtained with the diode bridge and different shunt values led to the calculation of the conversion efficiency by means of Eq. (19). As expected, short-circuit and open-circuit conditions lead to null conversion. Values in between these extremes yield the results in Fig. 11. From all the tested conditions, a shunt resistance of 465 mΩ guarantees the maximum conversion efficiency of 59.86%. However, this value is conservative because the mechanical power—the denominator of Eq. (19)—is overestimated. Moreover, the application of discrete shunt loads does not allow matching with precision the value that optimizes conversion efficiency. Despite these limitations, the RRSA prototype exhibits fairly low mechanical losses, which in turn lead to high conversion efficiency values.

When compared to other regenerative damper technologies, these numbers appear to be promising. In literature, efficiency values of electro-hydrostatic dampers rarely overcome 40% [11, 12]. Furthermore, their performance is affected by two types of losses: mechanical and volumetric. This shortcoming leads to very narrow regions of high efficiency, even in the best cases. On the contrary, our RRSA prototype exhibits efficiencies above 50% between 0.12 and 0.9 m/s when shunted with 465 mΩ.

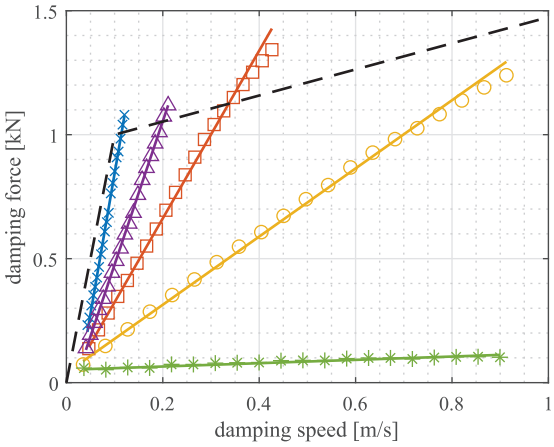

Figure 10: Experimental damping force characterization for different speed values with different shunt resistances: open circuit (asterisk), 465 mΩ (circle), 135 mΩ (square), 55 mΩ (triangle) and short circuit (cross). Experimental results are interpolated using a first-degree polynomial (solid) and can be compared to the damping specification (dashed).

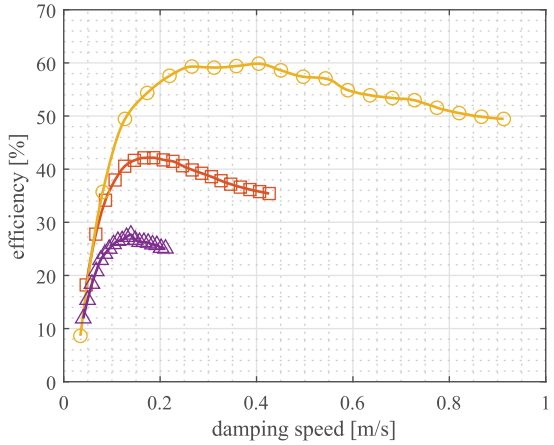

Figure 11: Experimental conversion efficiency characterization with shunt resistances of 465 mΩ (circle), 135 mΩ (square), 55 mΩ (triangle). Experimental results are treated with a shape-preserving interpolating polynomial function (solid).

State-of-the-art electromechanical solutions show mechanical efficiency values between 60 and 70% [6, 10]. These values are certainly lowered when the efficiency of the electric machine is taken into account.

3.3. Acoustic characterization

As previously stated, noise and vibration harshness (NVH) are critical aspects to consider in vehicle systems. As such, the RRSA was tested inside an anechoic chamber to evaluate the noise levels that it produces without the influence of sound reflections.

In the setup of Fig. 12, the prototype was placed over a foam layer with two microphones (AVM MI 17 1/4", free-field) aiming at one meter of distance from its front and side. The microphones were sampled at 12.8 kHz through the 24-bit analogue channels of LMS SCADAS data acquisition hardware.

The time-domain signals of both sensors were filtered using the A-weighting continuous-time function [38]

$$H_A(s) = \frac{7.4 \cdot 10^9 \cdot s^4}{(s+12.4)^2(s+7.7\cdot 10^4)^2(s+4.6\cdot 10^3)(s+676.7)} \tag{20}$$

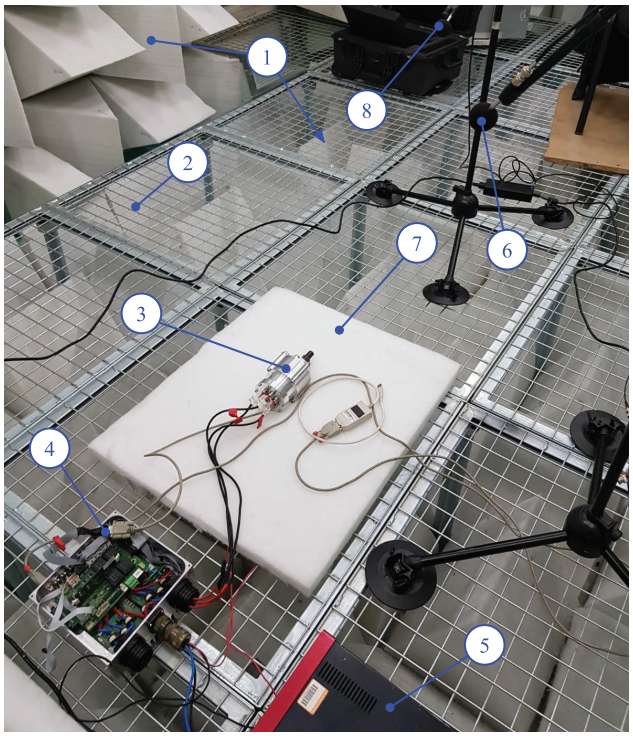

Figure 12: Experimental setup for acoustic characterization: wall and floor foam blocks (1), supporting structure (2), rotary regenerative damper prototype (3), prototype control unit (4), power supply (5), side microphone (6), foam pad (7), front microphone (8).

which is a common method to assess human sensitivity to noise levels. The filtered signals were then expressed as sound pressure levels (SPL) in dBA referenced to $p_0 = 20\,\mu$Pa:

$$SPL = 20\log_{10}\left(\frac{p_A}{p_0}\right) \tag{21}$$

where p_A is the A-filtered front/side acoustic pressure signal.

Acoustic measurements using the complete test setup in Fig. 9 would have included spurious noise components beyond those of the RRSA prototype. For this reason, the RRSA electric machine was driven as a motor using a dedicated power stage and supply. It was controlled with constant and sinusoidal speed references. The attained RMS SPL values for both of these inputs are detailed in Tab. 5. For clarity, the speed is expressed in the linear domain.

In general, it can be seen that side measurements are slightly larger than front ones. As expected, sinusoidal inputs yield lower sound pressure levels. It is worth noting that at speeds below 100 mm/s, where the suspension duty cycle

Table 5: Measured sound pressure levels with constant and sinusoidal input speeds.

Input type	Speed		RMS SPL [dBA]	
	amp. [mm/s]	freq. [Hz]	front	side
Constant	96	–	36.03	36.92
	178	–	42.3	44.08
	341	–	47.89	49.63
Sinusoidal	41	2	37.07	35.23
	62	1.5	37.01	37.36
	328	1	46.97	48.69

is predominant, the noise does not exceed 40 dBA. In the worst case, when reaching a constant speed of 341 mm/s, the noise level becomes 49.63 dBA on the side microphone.

As a reference, the United States Environmental Protection Agency establishes a 24-hour exposure limit of 55 dBA [39]. A more complete analysis is needed to understand the impact of using four RRSA devices in a vehicle. In such scenario, the mechanical interface between the device and the chassis has a strong influence on the transmission of vibrations, as well as the media used to isolate the cabin from the chassis components.

4. Conclusions

The present paper described a design methodology for a rotary regenerative shock absorber. It addressed the integrated sizing of electric machine, leverage and gearbox.

The followed procedure yielded a prototype with mass of 3.51 kg including the lever arm, maximum damping of 11.32 kNs/m, maximum damping-to-mass ratio of 3.23 kNs/(mkg) and maximum conversion efficiency of 59.86%. Through an experimental campaign, it was demonstrated that the rotary technology clearly outperforms alternative state-of-the-art solutions in all these metrics. Furthermore, in the acoustic domain, it was shown that the prototype does not exceed the standard noise limitations.

These results arise from a system-level approach that identified the maximum damping and the envelope dimensions of the device as input parameters. The method then used these inputs to size the electric machine in terms of cross section and active length, while also setting the overall transmission ratio of the system. The design was completed with the definition of a proper kinematic linkage between the device and the suspension, which in turn also set the transmission ratio of the gearbox.

Acknowledgment

The authors would like to gratefully thank Piero Conti, Giordano Greco, Andrea Nepote, Marco di Vittorio and Fabio Cotto from Magneti Marelli Shock Absorbers for their valuable support throughout this research activity.

References

[1] European Commission, Regulation no. 443 setting emission performance standards for new passenger cars as part of the community's integrated approach to reduce CO2 emissions from light-duty vehicles (2009).

[2] P. Múčka, Energy-harvesting potential of automobile suspension, Vehicle System Dynamics 54 (12) (2016) 1651–1670. doi:10.1080/00423114.2016.1227077.

[3] M. A. Abdelkareem, L. Xu, M. K. A. Ali, A. Elagouz, J. Mi, S. Guo, Y. Liu, L. Zuo, Vibration energy harvesting in automotive suspension system: A detailed review, Applied Energy 229 (2018) 672–699.

[4] B. L. Gysen, T. P. van der Sande, J. J. Paulides, E. A. Lomonova, Efficiency of a regenerative direct-drive electromagnetic active suspension, IEEE Transactions on Vehicular Technology 60 (4) (2011) 1384–1393.

[5] N. Amati, A. Festini, A. Tonoli, Design of electromagnetic shock absorbers for automotive suspensions, Vehicle System Dynamics 49 (12) (2011) 1913–1928.

[6] Y. Liu, L. Xu, L. Zuo, Design, modeling, lab, and field tests of a mechanical-motion-rectifier-based energy harvester using a ball-screw mechanism, IEEE/ASME Transactions on Mechatronics 22 (5) (2017) 1933–1943.

[7] Y. Kawamoto, Y. Suda, H. Inoue, T. Kondo, Electro-mechanical suspension system considering energy consumption and vehicle manoeuvre, Vehicle System Dynamics 46 (sup1) (2008) 1053–1063. doi:10.1080/00423110802056263.

[8] A. Tonoli, N. Amati, J. G. Detoni, R. Galluzzi, E. Gasparin, Modelling and validation of electromechanical shock absorbers, Vehicle System Dynamics 51 (8) (2013) 1186–1199.

[9] Z. Zhang, X. Zhang, W. Chen, Y. Rasim, W. Salman, H. Pan, Y. Yuan, C. Wang, A high-efficiency energy regenerative shock absorber using supercapacitors for renewable energy applications in range extended electric vehicle, Applied Energy 178 (2016) 177–188.

[10] Z. Li, L. Zuo, J. Kuang, G. Luhrs, Energy-harvesting shock absorber with a mechanical motion rectifier, Smart Materials and Structures 22 (2) (2012) 025008.

[11] Y. Zhang, H. Chen, K. Guo, X. Zhang, S. E. Li, Electro-hydraulic damper for energy harvesting suspension: Modeling, prototyping and experimental validation, Applied Energy 199 (2017) 1–12.

[12] R. Galluzzi, Y. Xu, N. Amati, A. Tonoli, Optimized design and characterization of motor-pump unit for energy-regenerative shock absorbers, Applied Energy 210 (2018) 16–27.

[13] R. Galluzzi, A. Tonoli, N. Amati, Modeling, Control, and Validation of Electrohydrostatic Shock Absorbers, Journal of Vibration and Acoustics 137 (1) (2015) 011012.

[14] M. Willems, Wheel suspension for a motor vehicle, uS Patent 8,573,604 (2013).

[15] B. Turkus, Audi is working on a suspension that gets power from bumpy roads, On the WWW, uRL http://www.autoblog.com (2016).

[16] Audi AG, Multifaceted personality: predictive active suspension in the A8 flagship model., On the WWW, uRL http://www.audi-mediacenter.com (2019).
[17] U. K. Lee, Energy regeneration device of suspension system for vehicle, uS Patent App. 13/238,302 (2012).
[18] Y. Matsuoka, Vehicle suspension system using a rotary damper, uS Patent 5,074,581 (1991).
[19] K. Deb, S. Jain, Multi-Speed Gearbox Design Using Multi-Objective Evolutionary Algorithms, Journal of Mechanical Design 125 (3) (2003) 609–619. doi:10.1115/1.1596242.
[20] P. Lynwander, Gear drive systems: Design and application, CRC Press, Boca Raton, FL, USA, 2019.
[21] Y.-J. Park, G.-H. Lee, J.-S. Song, Y.-Y. Nam, Characteristic Analysis of Wind Turbine Gearbox Considering Non-Torque Loading, Journal of Mechanical Design 135 (4) (2013) 044501. doi:10.1115/1.4023590.
[22] H. Khakpour Nejadkhaki, A. Lall, J. F. Hall, A Methodology to Synthesize Gearbox and Control Design for Increased Power Production and Blade Root Stress Mitigation in a Small Wind Turbine, Journal of Mechanical Design 139 (8) (2017) 081404. doi:10.1115/1.4036998.
[23] D. C. Hanselman, Brushless Permanent Magnet Motor Design, Magna Physics Publishing, Lebanon, OH, USA, 2006.
[24] D. G. Dorrell, M.-F. Hsieh, M. Popescu, L. Evans, D. A. Staton, V. Grout, A Review of the Design Issues and Techniques for Radial-Flux Brushless Surface and Internal Rare-Earth Permanent-Magnet Motors, IEEE Transactions on Industrial Electronics 58 (9) (2011) 3741–3757.
[25] ISO 8608:1995, rev. 2011. Mechanical vibration – road surface profiles – reporting of measured data.
[26] L. Zuo, P.-S. Zhang, Energy harvesting, ride comfort, and road handling of regenerative vehicle suspensions, Journal of Vibration and Acoustics 135 (1) (2013) 011002.
[27] A. Tonoli, Dynamic characteristics of eddy current dampers and couplers, Journal of Sound and Vibration 301 (3-5) (2007) 576–591.
[28] A. Tonoli, N. Amati, Dynamic Modeling and Experimental Validation of Eddy Current Dampers and Couplers, Journal of Vibration and Acoustics 130 (2) (2008) 021011.
[29] K. R., Permanent Magnet Synchronous and Brushless DC Motor Drives, CRC Press, Boca Raton, FL, USA, 2010.
[30] S. S. Balli, S. Chand, Transmission angle in mechanisms (triangle in mech), Mechanism and Machine Theory 37 (2) (2002) 175–195.
[31] J. C. Dixon, The Shock Absorber Handbook, John Wiley and Sons, Ltd., 1999.
[32] ISO 6336-1:2006. Calculation of load capacity of spur and helical gears – Part 1: Basic principles, introduction and general influence factors.
[33] ISO 6336-1:2006. Calculation of load capacity of spur and helical gears – Part 2: Calculation of surface durability (pitting).
[34] ISO 6336-1:2006. Calculation of load capacity of spur and helical gears – Part 3: Calculation of tooth bending strength.
[35] ISO 6336-1:2006. Calculation of load capacity of spur and helical gears – Part 6: Calculation of service life under variable load.
[36] J. E. Shigley, Shigley's mechanical engineering design, Tata McGraw-Hill Education, NY, USA, 2011.
[37] KISSSoft A.G., KISSSoft Release 03/2017 User Manual (2017).
[38] DIN EN 61672-1: 2014-07. Electroacoustics – Sound level meters – Part 1: Specifications.
[39] M. S. Hammer, T. K. Swinburn, R. L. Neitzel, Environmental noise pollution in the united states: developing an effective public health response, Environmental health perspectives 122 (2) (2013) 115–119.